UNDERSTANDING SUBSURFACE PATTERNS OF SUSPENDED SEDIMENT IN TIDAL SEAS THROUGH SATELLITE IMAGERY, SOUTH KOREA

by

Catherine Evans

Submitted in partial fulfillment of the requirements
for the degree of Master of Science

at

Dalhousie University
Halifax, Nova Scotia
October 2022

An ocean (or macrotidal shallow sea's worth) of thanks to Dr. Paul Hill, for the weekly Zoom meetings, guidance, and DIY project comparisons through the many COVID waves these past few years. You've been a fantastic supervisor and mentor through both this degree and my undergraduate thesis.

To Dr. Dan Kelley and Dr. Tim Milligan, for the stories, papers, insightful questions, and intelligent discussions, which have made me a better scientist.

To the Oceanography Department, for the kindness, exchanging of ideas, and consistently welcoming atmosphere.

To the Office of Naval Research, for providing the funding for this project.

And to all of my loved ones, for the cheer, food, work sessions, outdoor adventures, affection, and laughter.

Table of Contents

List of Tables

List of Figures

Abstract

Banded patterns in remotely sensed reflectance can correlate with bathymetry in macrotidal seas. Over ridges, reflectance is higher, and over adjacent channels it is lower. This may be due to faster current speeds at shallower depths. Alternatively, depth-dependant stratification could limit upward mobility of sediment in tidal channels. Evidence of stratification over the Heuksan Mud Belt (HMB) off southwest Korea was examined by analyzing GOCI time series of Rayleigh-corrected reflectance. Reflectance measurements were fitted to a M4 periodic function, simulating flows of the HMB's M2 constituent tide. Phase lag of peak reflectance in relation to high tide was related to depth, generating regional estimates of vertical eddy diffusion coefficients. The coefficient was consistent with theoretical values of an unstratified environment in the spring and summer, and lower in the fall and winter. This difference suggests seasonal stratification, caused by changes in suspended sediment concentration related to the East Asian Monsoon.

Chapter 1

Introduction

1.1 Suspended Sediment in Macrotidal Seas

In macrotidal shelf seas, bathymetry is often characterized by sets of sediment ridges oriented obliquely to the tidal flow (28). In these regions, which have high current speeds and large concentrations of suspended sediment, similar linear patterns of remotely-sensed reflectance in the red wavelength occur ($\sim$ 660 nm) (2; 9; 34). Reflectance correlates with bathymetry, with higher reflectance over ridges, and lower reflectance over adjacent channels (2; 9). Reflectance of red light commonly is used as a proxy for suspended sediment in water, so high reflectance indicates high suspended sediment concentration (SSC). Banded reflectance that correlates with bathymetry is apparent at many locations around the globe, for example in the Bay of Khambhat on the west coast of India, in the Wash on the east coast of the United Kingdom, in Bristol Bay in Alaska, in the Gulf of California, and off the west coast of Korea (Figures 1.1-1.3)

A relatively simple explanation of the correlation between reflectance and bathymetry is that currents are faster over ridges than channels. If the volume transport of water over a channel and a ridge is the same, then water must move faster over the ridge because water column is shallower. If water flows faster over ridges, then more sediment is re-suspended by the tidal flow, causing a higher reflectance at the water's surface (2; 34).

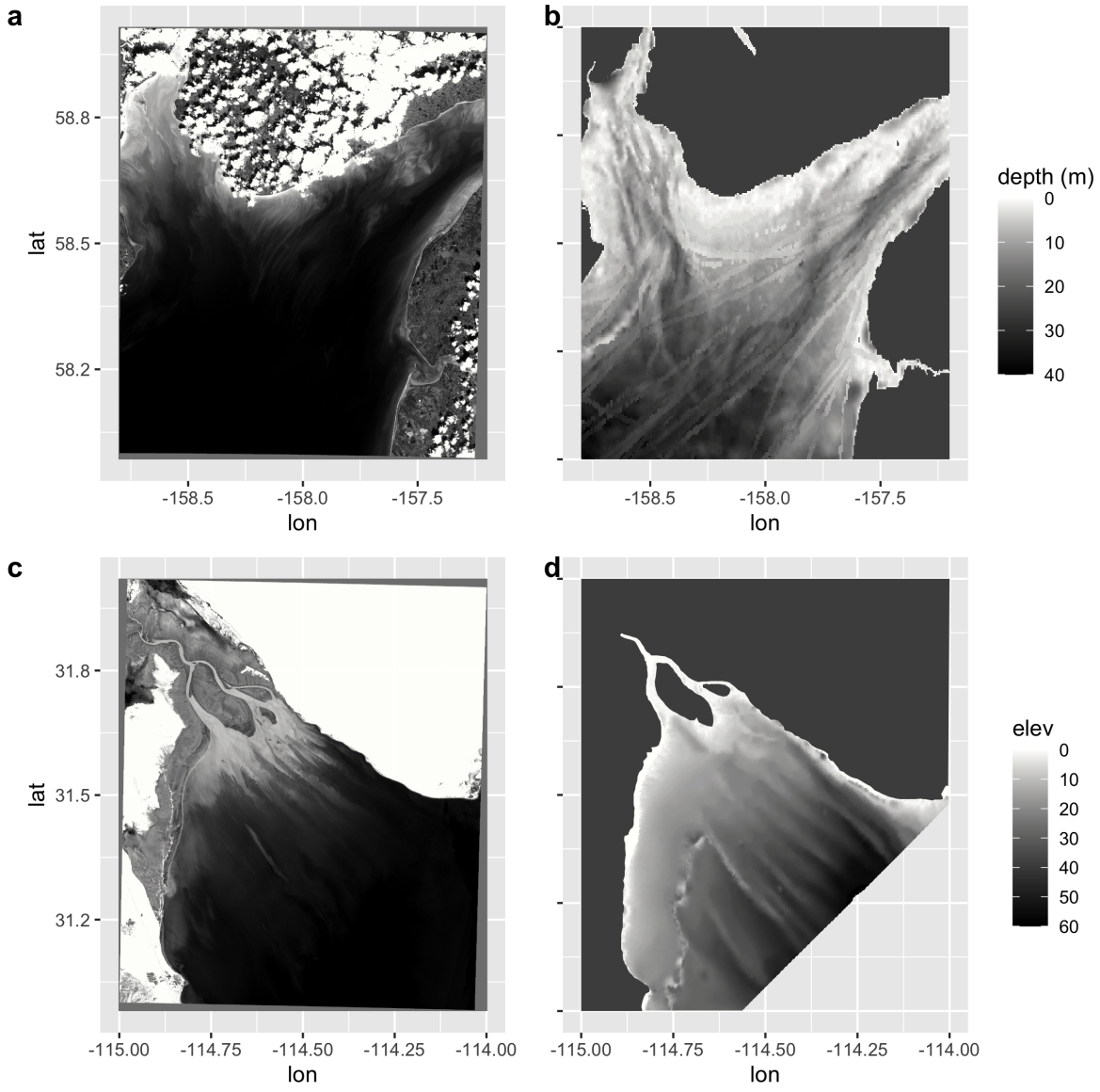

Figure 1.1: Landsat imagery and bathymetric maps of macrotidal regions around the world. Patterns of surficial SSC - which can be measured by Landsat's band 4 - correlate with the underlying bathymetry in each area. Ridges tend to have a higher reflectance than surrounding channels when tidal currents are flowing. A) Landsat band 4 image of Cook Inlet, off the Alaskan coast. B) Bathymetry of Cook Inlet. C) Landsat band 4 Image of the Gulf of California, United States. D) Bathymetry of the Gulf of California.

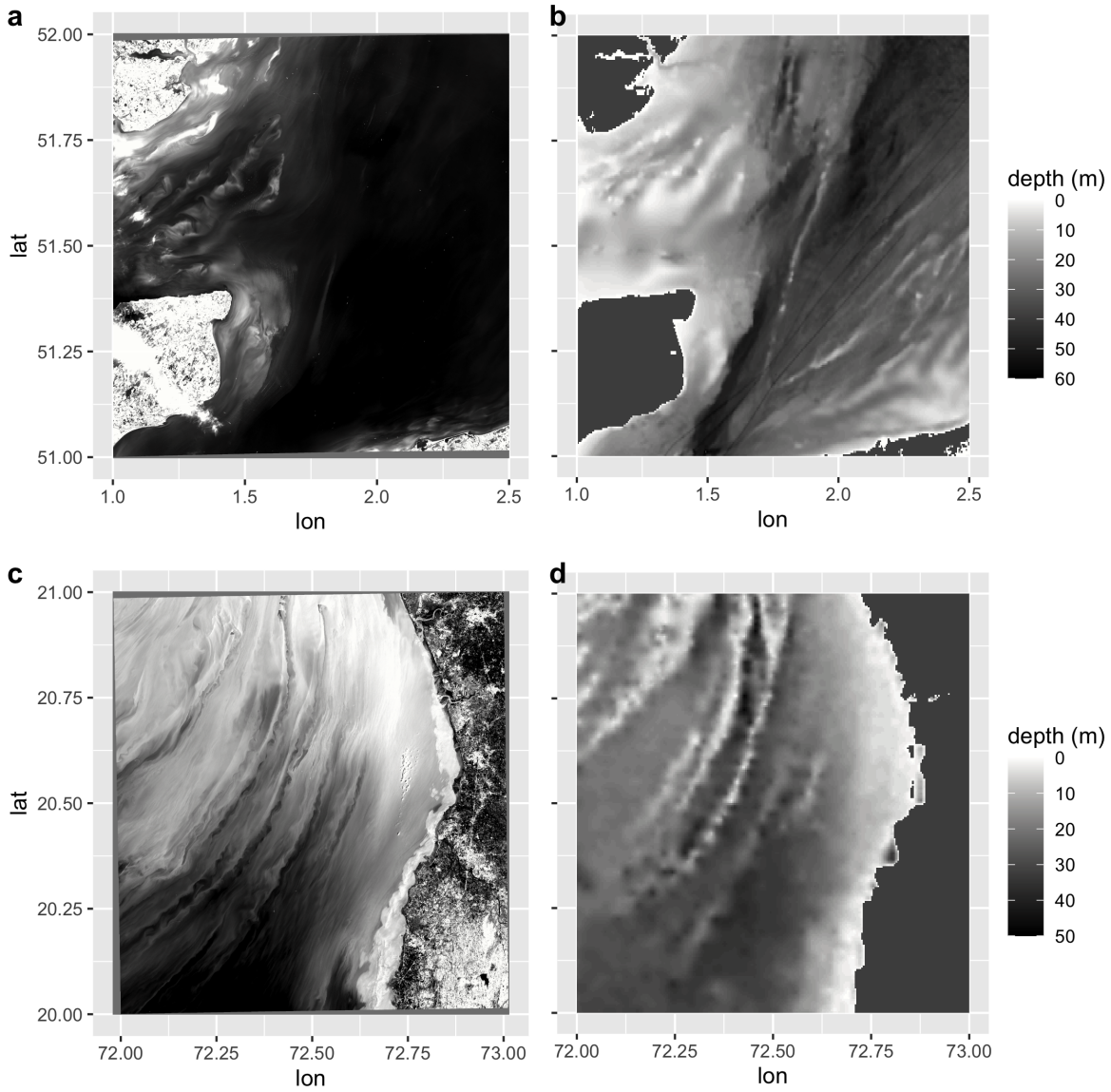

Figure 1.2: Landsat imagery and bathymetric maps of macrotidal regions around the world. See Figure 1 for explanation. a) Landsat band 4 image of The Wash, off England's east coast in the North Sea. b) Bathymetry of The Wash. c) Landsat band 4 image over the Gulf of Khambhat, India. d) Bathymetry of the Gulf of Khambhat.

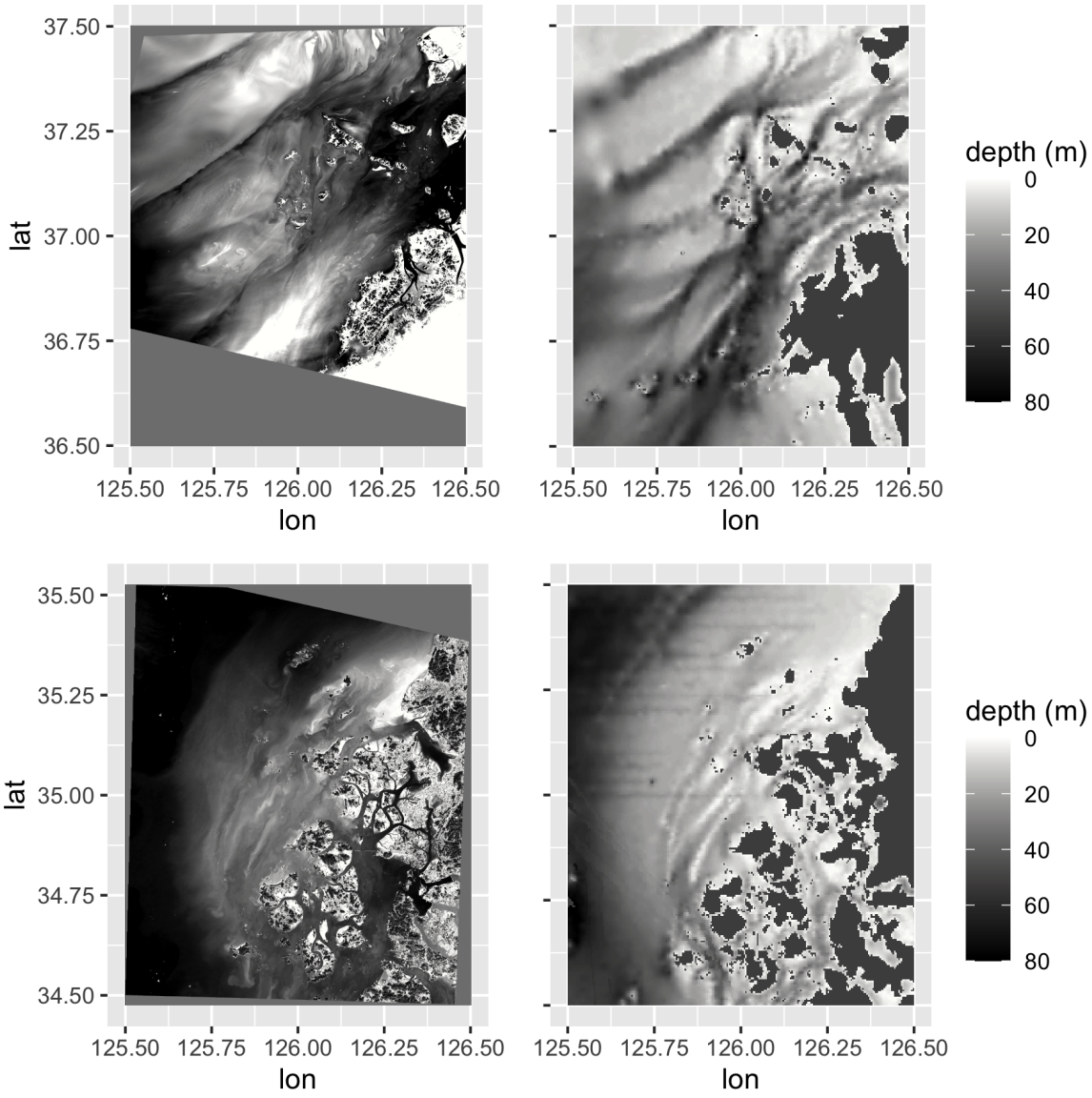

Figure 1.3: Landsat imagery and bathymetric maps of macrotidal regions around the world. See Figure 1 for explanation. a) Landsat band 4 image of Gyeonggi Bay, South Korea. b) Bathymetric map of Gyeonggi Bay. c) Landsat band 4 image over the Heuksan Mud Belt of the South Korean coast. d) Bathymetry of the Heuksan Mud Belt and surrounding region.

The above explanation may be too simple. The seabed stresses in macrotidal seas are large both in the channels and over the ridges, so the differences in suspended sediment concentration may not be large enough to produce the observed banded pattern of reflectance without other subsurface processes affecting sediment uplift (2). Furthermore, the seabed sediment in channels has been observed to be finer than on the ridges (28). Given that finer sediment is more erodible, then differences between reflectance over the ridges and over the channels would be reduced.

An alternative explanation for the correlation between bathymetry and reflectance in macrotidal seas is that mixing of suspended sediment to the sea surface is suppressed by stratification in the tidal channels. These environments experience strong currents and are well mixed in temperature and salinity, so T-S stratification is unlikely. Stratification could arise, however, from density stratification induced by large nearbed concentrations of suspended sediment (33; 1). Stratification could be localized to channels because dense suspensions that form over ridges would flow laterally into channels under the influence of gravity.

The effects of stratification on the time-varying concentration of suspended sediment in a tidal flow can be investigated analytically with simplified models (38). Under the assumptions of horizontal uniformity and a depth-invariant eddy diffusion coefficient, suspended sediment concentration (SSC) ($C(z,t)$) as a function of time (t) and height (z) above the seabed is described by the equation

$$C(z,t) = N * \exp(-\frac{w_s}{K_s}z) + N * \exp(-a\frac{w_s}{K_s}z)\cos(2t\omega - b\frac{w_s}{K_s}z), \tag{1.1}$$

where w_s is sediment settling velocity (mm s^{-1}), K_s represents the vertical eddy diffusion coefficient (m^2 s^{-1}), and ω is tidal frequency (s^{-1}). The coefficient N is average sediment concentration at the bottom boundary over a course of a tidal cycle. The coefficients a and b are defined by

$$a = (1 + \sqrt{1 + 4b^2})/2,$$

$$b = \left(\frac{1 + \sqrt{1 + 64\omega^2 K_s^2 / w_s^4}}{8} \right)^{1/2} \tag{1.2}$$

Equation 1.1 can be broken down into two parts. The first term on the right hand side is independent of time, and it defines the exponential decrease of SSC with increasing height from the seabed. The second term defines the M4 periodic variability of the sediment concentration profile. The lag in the cos term equals ($b\frac{W_s}{K_s}z$), demonstrating that phase lag of sediment increases with height z above the seabed. Both the exponential decrease with height above the bed and the phase depend on the ratio of sediment settling velocity to the eddy diffusion coefficient. These dependencies show that if the eddy diffusion coefficient is reduced because of stratification, then the concentration at height z will be smaller, and the time required for sediment resuspended from the bed to reach that height will be larger (Figure 1.4). Therefore, analysis of the phase lag of surface sediment concentration offers a means of assessing the possible role of stratification in creating the banded reflectance patterns in macrotidal shelf seas. The goal of this research is to assess the potential role of suspended sediment stratification by examining the dependence on depth of the time required for sediment to reach the water's surface using high-frequency satellite imagery.

1.2 Satellite Remote Sensing

Correlations between bathymetry and reflectance patterns are apparent in Landsat imagery (Figures 1.1-1.3). Satellites such as Landsat or Sentinel, however, do not have the return times needed to observe surficial patterns throughout a tidal cycle, as the return time over a location can range from days to weeks. In order to observe surface patterns throughout the tidal cycle in one of the locations where banding has been observed, a satellite would need to be able to take multiple images throughout the day. The satellite would also need a resolution fine enough

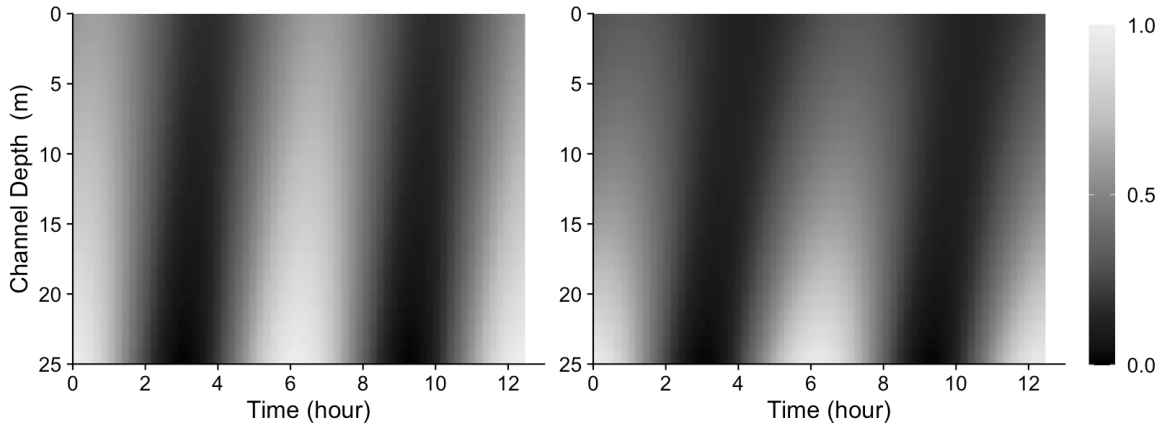

Figure 1.4: Model (Yu et al., 2011) time series of SSC concentration in the water column throughout a tidal cycle. **Left**: Time series with an eddy diffusivity value based on an average flow speed of 0.75 m s^{-1} and flow depth of 25 m. **Right**: Time series with an eddy diffusivity ten times smaller to illustrate the effects of density stratification. In the stratified case, surface SSC levels are lower, and there is greater lag in the arrival of peak SSC at the surface after peak flow.

to resolve the banded reflectance patterns. The Geostationary Ocean Color Imager (GOCI) located over the Korean peninsula provides the temporal and spatial resolution required to carry out the analysis (30).

GOCI is the world's first optical geostationary ocean color device. The imager is part of the Communication, Ocean, and Meteorological Satellite (COMS), and it was in operation from April 2011 until early 2021 (30). The sensor processes 8 different bands in both visible and near infrared wavelengths [Table 1.1]. GOCI captures 8 images daily, in hourly intervals from approximately 9:00 AM - 4:00 PM KST (30). The objective of this research is to use sequences of GOCI images to examine the depth dependence of phase lag in reflectance at the sea surface. This dependence is used to constrain the values of the vertical eddy diffusion coefficient, so comparison can be made to theoretical values for stratified and unstratified flows.

Band no.	**Wavelength λ (nm)**	**Band Use Description**
1	412	Yellow substance, turbidity
2	443	Chlorophyll absorption maximum
3	490	Chlorophyll and other pigments
4	555	Turbidity, suspended sediment
5	660	Baseline of fluorescence, chlorophyll, suspended sediment signal
6	680	Atmospheric correction and fluorescence signal
7	745	Atmospheric correction and baseline of fluorescence signal
8	865	Aerosol optical thickness, vegetation, water vapor reference over the ocean

Table 1.1: Condensed version of Ryu's summary table on characteristics of GOCI's spectral bands

Chapter 2

Methods

2.1 Site Description

Strong tidal currents have formed shore-parallel ridges and channels off of South Korea's west coast, which is an area imaged by GOCI. Tidal ranges in the region range between mesotidal and macrotidal, with spring tides that can exceed a range of 5 meters, and peak current speeds ranging between 1-2 m s^{-1} (16; 8; 23). The currents are dominated by the M2 tidal constituent, meaning two tidal cycles per day, and four periods of peak flow, with one on each of the two flooding tides and one on each of the ebbing tides. Both temperature and salinity are nearly constant through the water column from strong tidal mixing and mixing by waves (22; 23).

On the seabed in this region is a Holocene deposit called the Heuksan Mud Belt (HMB). The distinctive ridges and channels of the HMB formed during the rise in sea level since the last glacial maximum, beginning at approximately 16 ka (22; 21). The study area focuses on a portion of the HMB's shallow marine waters, with a maximum water depth of approximately 50 m, between the coordinates of $34.8 - 35°$N, $125.8 - 126°$ E (Figure 2.2). The HMB is characterized by high levels of loose, fine sediment along its seabed. Sediment ranges from fine muds to fine sands, and is mobilized by tidal currents and wind-derived wave action, which creates a turbid environment (14; 22; 16).

2.1.0.1 Seasonal Dynamics over the HMB

South Korea experiences the seasonal effects of the East Asian monsoon. In the summer, warm air from the Pacific Ocean blows from the southeast over the Korean Peninsula (37). Tide flats along the coast adjacent to the HMB are sheltered from waves due to the wind's prevailing direction (Figure 2.1). The relative lack of wave energy allows sediment to deposit seasonally on the tide flats (16). In winter winds tend to blow from the northwest. The tide flats adjacent to the HMB are not sheltered from waves generated by winds from this direction (Figure 2.1). The large wind fetch down the length of the Yellow Sea increases wave energy impinging on the shallow seabed in the area (37). Increased wave energy leads to erosion of sediments deposited during summer. The strong northern winds also create a seasonal current - the Korean Coastal Current - that flows southward along Korea's west coast. The Korean Coastal Current is the primary modern mode of transport and deposition of a new supply of suspended sediment over the HMB (21).

Precipitation over the Korean peninsula changes with the seasonal change in wind direction. Precipitation is highest from June to August (17; 37) (Figure 2.1). In these months, rivers along the coast flood and deposit large amounts of sediment along the coastline and within their respective estuaries (23). Of particular note is the Geum river, located approximately 150 km north of the study site, which supplies a seasonal deposit of fine sediment on the coastal tide flats during the months of high precipitation and associated river discharge (23; 16).

Tidal flats that develop through the summer erode in the fall and winter, and sediment is carried south over the HMB via a combination of increased stresses on the seabed and the strengthened, southward-flowing Korean Coastal Current (22; 23). Lee (2020) used GOCI observations to map a plume of sediment derived from the Geum River estuary over the HMB throughout the winter, providing a synoptic view of the seasonal mobilization of sediment, as well as documenting the HMB's primary modern sedimentary source (23).

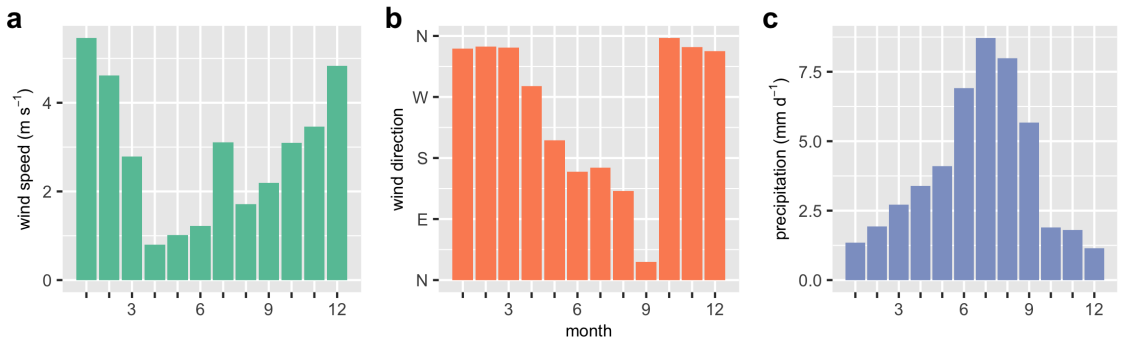

Figure 2.1: Wind speed, direction, and precipitation measurements throughout the year. **a**: Wind speed by month, showing that winds are strongest in the winter. **b**: Wind direction, showing a shift from southerly to northerly winds in the fall and winter **c**: Precipitation levels by month, showing that precipitation is largest in summer.

2.1.0.2 SSC over the HMB

Due to the seasonal dynamics, SSC over the HMB is lower in the summer than the winter, with in-situ surficial measurements of 2 g m^{-3} and 100g m^{-3} respectively (22). Lee (2001) also notes that SSC was higher at depth, varying from 100 g m^{-3} in summer to 350 g m^{-3} during the winter (22). Choi (2012) and Lee (2020) made similar observations of seasonal surficial SSC estimated remotely with GOCI. Choi's algorithm was able to estimate surface SSC up to 50 g m^{-3}, while Lee used an algorithm that allowed for estimations of surface concentrations exceeding 150 g m^{-3}. Both results were in agreement with Lee's (2001) in-situ data (5; 22; 23). GOCI reflectance measurements indicated that surficial SSC was lowest between the months of May to September, and built up to maximum concentrations between January and March (5; 23). SSC was lowest in August, with Choi noting a monthly average of only 10 g m^{-3} on the water's surface. Lee (2020) also noted that due to the prevailing southeasterly winds in summer, clear waters from the Pacific can be observed via GOCI imagery to flow into the West Sea and over the HMB, which would further dilute the surficial SSC (23).

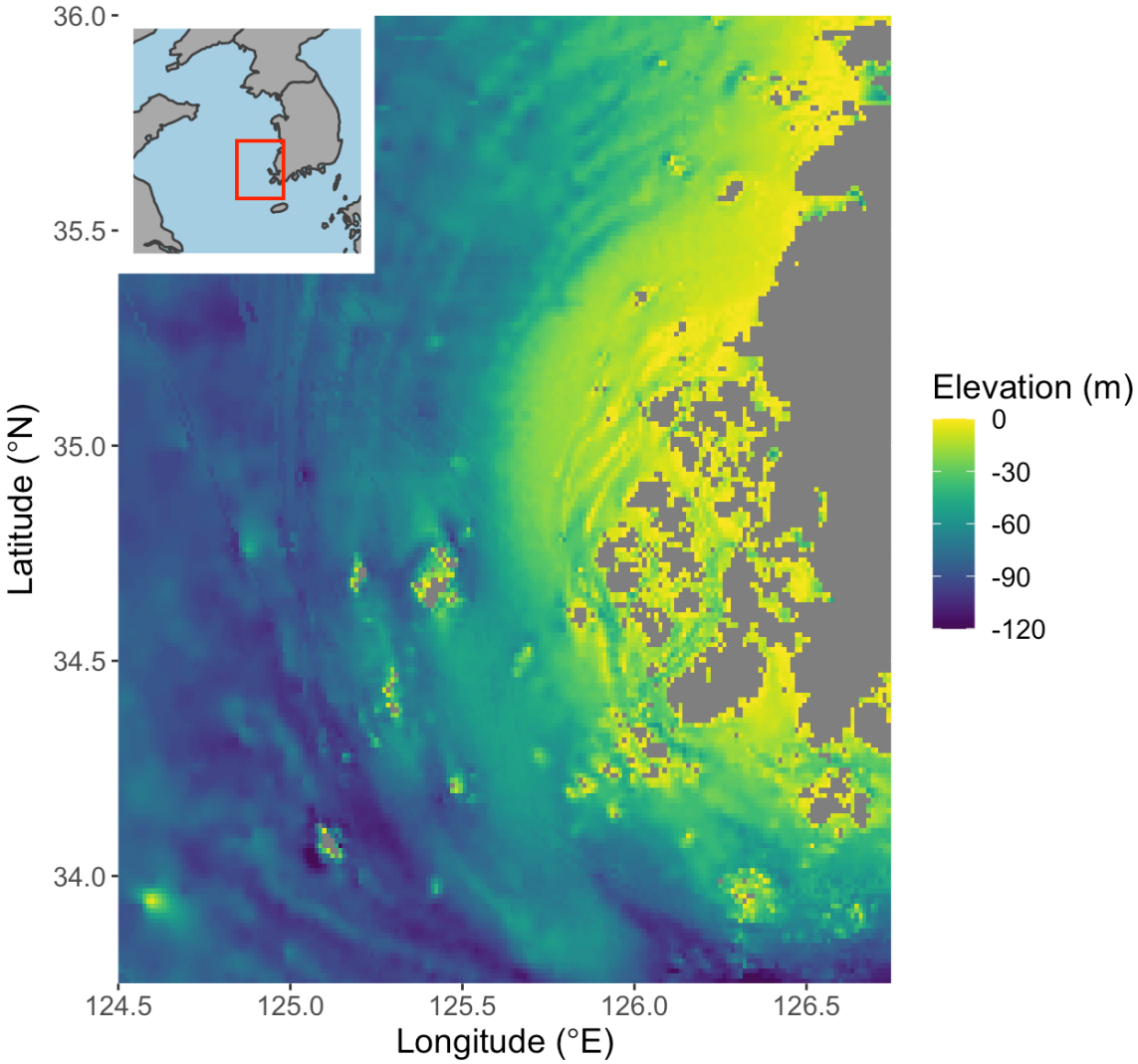

Figure 2.2: Regional bathymetry off the southwest coast of South Korea from the GEBCO 2020 grid (12). The area is characterized by a series of ridges, which run through an area of islands and parallel to the coast. The rectangle in the map inset outlines the study box.

2.2 Data Acquisition

GOCI images are available from NASA's OceanColor website (3). GOCI's daily capture of 8 images dates back to April 2011. Each day of images was viewed, and days with 8 cloud-free images over the study area were selected for analysis. Thirty-two days met this criteria, and Level 1 data for these days were downloaded.

GEBCO's Gridded Bathymetry Data is a free online data set that allows access to bathymetry and terrain elevation with a resolution of 15 arc-seconds (450 m) (12). A grid of the study area was downloaded as a GeoTIFF.

GOCI and GEBCO have different spatial resolutions. The GEBCO dataset was reprojected to the same resolution as the imagery by interpolating the GEBCO bathymetry measurements from its 450 m resolution to GOCI's 500 m resolution. This was done by taking the median depth between any GEBCO cells that fell within a GOCI pixel. Reprojecting bathymetry to GOCI's extent and resolution made it possible to compare reflectance measurements to water depth for each pixel of the GOCI images.

2.3 Rayleigh-Corrected Reflectance

Initial analysis relied on the Level 2 remotely-sensed reflectance product generated by the SeaDAS algorithms. Despite the clarity of the selected image sets, pixels frequently were masked as highly reflective clouds. Masking over turbid coastal waters is common in ocean colour algorithms, and it is due to complex atmospheric scattering conditions close to turbid water's surface, which causes the sensor to flag or misclassify the reflectance value (29).

As an alternative, Rayleigh-corrected reflectance from GOCI has been shown to correlate with turbidity in coastal waters off of Zhiengjiang Province in China (27), which is to the southwest of the study area. Rayleigh-corrected reflectance R_{rc} is defined as

$$R_{rc} = \frac{\pi(L_t - L_r)}{F0 * cos(\theta_o)}, \tag{2.1}$$

where L_t, the total top-of-atmosphere radiance measured by the sensor, L_r (W m^{-2}) is the Rayleigh radiance caused by scattering from air molecules, θ_o is the solar zenith angle and $F0$ (W m^{-2}) is solar irradiance at the top of the atmosphere, which has a value of 1563 mW m^{-2} nm^{-1} a wavelength of at 660 nm (32). Level 1 GOCI imagery was processed using NASA's SeaDAS package. The l2gen tool was used to generate values for L_t, L_r and θ_o for each image.

2.4 Model Fitting

Under the assumptions that tidally induced stress at the seabed is responsible for the resuspension of sediment and that Rayleigh-corrected reflectance in band 5 (red light, 660 nm) of GOCI varies primarily in response to suspended sediment concentration at the sea surface, R_{rc} data for each 8-image set were fitted to an M4 periodic function. The M4 periodicity was assumed because sediment is suspended both on the flooding and ebbing tides.

The temporal variability of R_{rc} is assumed to follow the equation

$$R_{rc} = \overline{R_{rc}} + A\sin(\omega t + \phi), \tag{2.2}$$

where $\overline{R_{rc}}$ is the mean Rayleigh-corrected reflectance for an 8-image set, ω is the M4 radian frequency equal to $3 \times 10^{-4} s^{-1}$, t is time from high tide and ϕ is the phase. To solve for ϕ, the $\sin$ term is replaced with the identity

$$\sin(\omega t + \phi) = \cos(\omega t)\sin(\phi) + \sin(\omega t)\cos(\phi). \tag{2.3}$$

Substitution of this identity into equation 2.2 yields

$$R_{rc} = \overline{R_{rc}} + A\cos(\omega t)\sin(\phi) + A\sin(\omega t)\cos(\phi). \tag{2.4}$$

To simplify notation, let

$$\begin{aligned} y &= R_{rc}; \\ b &= \overline{R_{rc}}; \\ x_1 &= \cos(\omega t); \\ m_1 &= A\sin(\phi); \\ x_2 &= \sin(\omega t); \\ m_2 &= A\cos(\phi). \end{aligned} \tag{2.5}$$

With these substitutions equation 2.4 becomes

$$y = b + m_1 x_1 + m_2 x_2. \tag{2.6}$$

The coefficients b, m_1 and m_2 were determined by the linear regression of y on x_1 and x_2, and the coefficients were used to solve for the amplitude and phase of the $\sin$ function that was fit to the GOCI data.

Noting that

$$m_1^2 + m_2^2 = A^2(\sin^2(\phi) + \cos^2(\phi)) = A^2, \tag{2.7}$$

the solution for A is as follows:

$$A = \sqrt{m_1^2 + m_2^2}. \tag{2.8}$$

The ratio of m_1 to m_2 is

$$\frac{m_1}{m_2} = \frac{A\sin\phi}{A\cos\phi} = \tan\phi, \tag{2.9}$$

so the phase equals

$$\phi = \arctan\frac{m_1}{m_2}. \tag{2.10}$$

If m_1 was positive and m_2 was negative, π was added to the phase. If both m_1 and m_2 were negative, π was subtracted from the phase.

Times in the model were referenced to the time of high tide in the study box. The Oregon

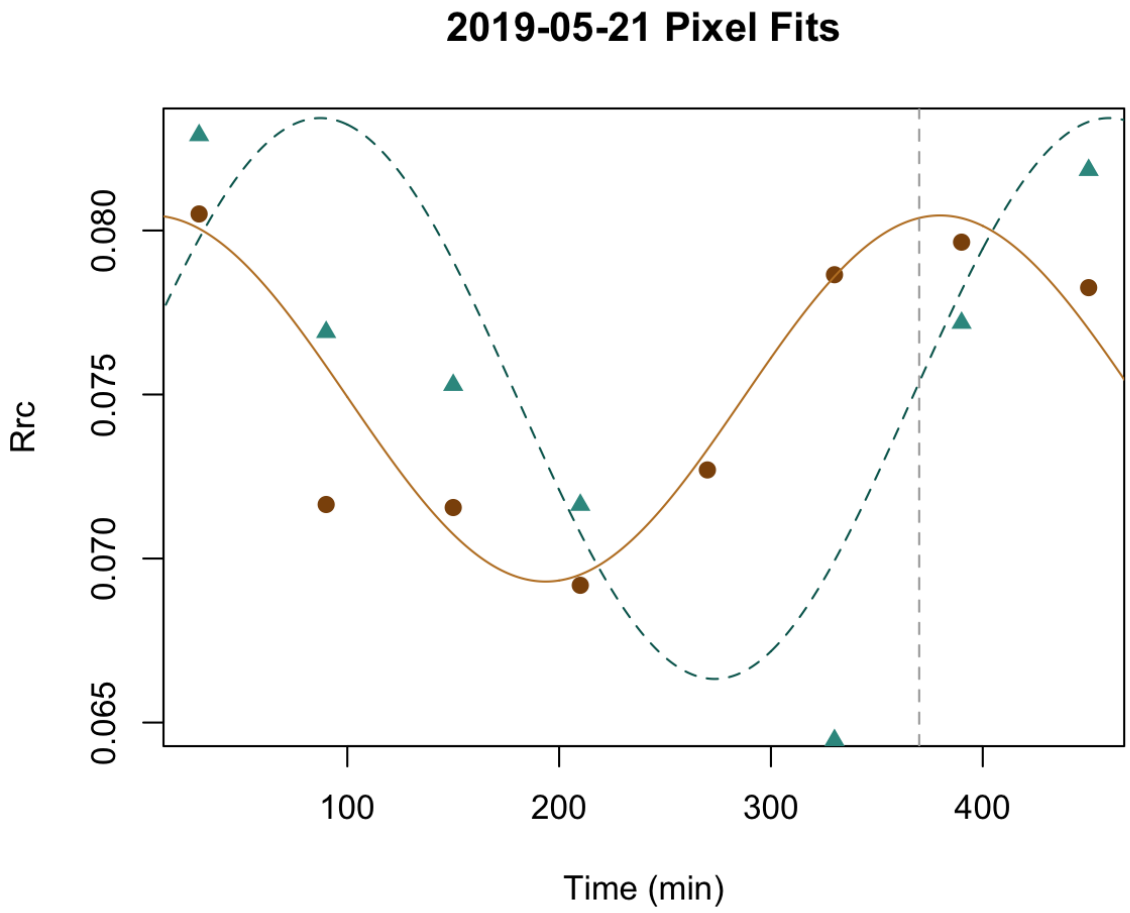

Figure 2.3: Example fits of a periodic function with M4 tidal frequency to time series of Rayleigh-corrected reflectance values at pixels located over shallower (13 m, brown) and deeper (22 m, blue) water in the study box. Phase of the fits is referenced to time of high tide, which is indicated by a vertical line.

State University Tidal Prediction Software (OTPS) was used in conjuntion with MATLAB's Tidal Model Driver (TMD) toolbox to predict water levels with 10-minute resolution on each of the 32 days with clear image sets (26). Tides were predicted at the coordinates $34.888°N$, $125.855°E$, a location near the centre of the study box where fieldwork was conducted in 2017 (13).

2.5 Quality Control

To focus on image sets for which tides dominated the variability in reflectance, only days that had 300 or more pixels with fitted p values less than 0.05 were analyzed. Nine days passed these quality control criteria. This quality control helped remove days in which there may have been high winds, reducing the tidal signal because of sediment resuspension from wave action. It also excluded days on which a high tide occurred well outside of the image capture window. For the nine days, any pixels that were overlying depths shallower than 10 m were excluded in order to avoid reflectance from the seafloor or adjacency effects from land.

2.6 Eddy Diffusion from Phase

Equation 1.1 outlines how sediment concentration diffuses through the water column throughout a tidal cycle. The simplified model by Yu et al. below relates the vertical phase lag of suspended sediment rising from the seafloor to M4 tidal frequency (ω), eddy diffusion (K_s), and the height of the water parcel above the seabed (z) (38). This equation operates under the assumption that the settling velocity of suspended sediment is much smaller than K_s. The assumption is safe to make, due to the high current speeds and small sediment size in the region.

$$\phi(z) = \sqrt{\frac{\omega}{K_s}} z \tag{2.11}$$

The equation demonstrates that two locations that have the same tidal frequency and eddy diffusion values but different depths would have different phase lags. A deep channel has more water for suspended sediment to diffuse through than a ridge, resulting in suspended sediment taking more time to reach the water's surface.

Dependence of phase on depth was calculated for each image set that passed the quality control criteria. A quantile regression was performed on the phase and depth data from the pixels in an image set that showed M4 variability (18). A quantile fit was used rather than

a simple linear regression to reduce influence from outlier pixels on the fit. The quantile regression was performed on the median, with secondary regressions performed on the first and third quartile boundaries. Confidence intervals on the quantile regression were calculated with the bootstrap method, which re-samples the data set multiple times to create multiple estimates of the regression coefficients.

Based on Equation 2.11, an eddy diffusivity representative of the entire image can be estimated from the slope of the regression of phase on depth. The expression takes the form:

$$K_s = \frac{\omega}{m^2}, \tag{2.12}$$

where m is the slope of the regression.

Chapter 3

Results

3.1 Pixel Fits

On the nine days with significant M4 variability in Rayleigh-corrected reflectance, reflectance was inversely correlated with the underlying bathymetry. The intercepts of the fits at each pixel, which are equivalent to mean reflectance over the 8-image period, were higher in shallower regions of the study area than they were in deeper areas. Because Rayleigh-corrected reflectance in the red GOCI band is correlated with suspended sediment concentration at the surface (27), more suspended sediment was reaching the water's surface over ridges than channels.

The amplitudes of the model fits at each pixel were also inversely correlated with depth. Shallow ridges had higher fitted amplitudes than channels, indicating that there was more variation in the surface concentration of suspended sediment. Essentially more suspended sediment is both brought up to, but also sinks from, the water's surface over ridges.

Finally, phases of the model fits at each pixel also were correlated with depth. Phases were higher in shallower water than deeper water, which indicates that maximal reflectances over ridges generally led maximal reflectances over channels.

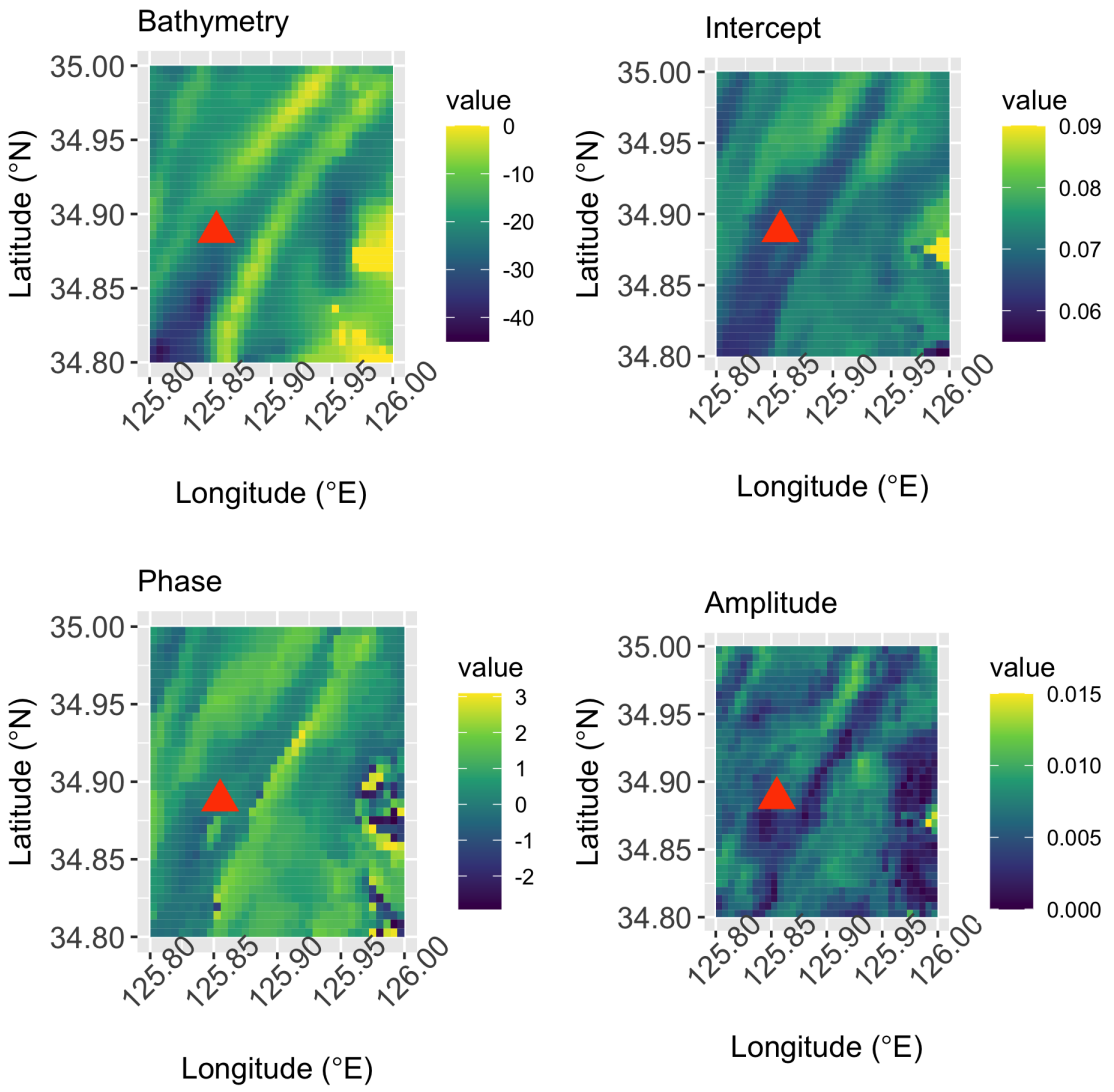

Figure 3.1: Spatial distribution of bathymetry and model parameters in the study box on May 21, 2019. **A)** GEBCO bathymetry, interpolated to the spatial resolution of GOCI imagery. **B)** Intercept from fitted wave, representing the mean Rayleigh-corrected reflectance for each pixel. **C)** Phase lag in relation to high tide. **D)** Amplitude of fitted wave. In accordance with model predictions, mean reflectance, phase and amplitude are lower in deeper water. Red triangle represents location of previous fieldwork conducted in 2017.

3.2 Eddy Diffusion Results

Applying Yu's equation to each of the quantile regression slopes of phase values gave three confidence intervals of eddy diffusion per day [Table 3.1].

Date	First Quartile	Second Quartile (Median)	Third Quartile
2012-03-26	0.0213	0.0785	1.1736
2019-05-21	0.0142	0.0246	0.0528
2019-05-22	0.0392	0.0746	0.1939
2019-05-23	0.0505	0.1000	0.2850
2011-07-19	0.0153	0.0428	0.3855
2013-09-16	0.0077	0.0099	0.0133
2013-10-04	0.0097	0.0179	0.0431
2018-11-02	0.0076	0.0105	0.0154
2020-11-11	0.0136	0.0240	0.0529

Table 3.1: Calculated Eddy Diffusion values calculated from median, first, and third quantile regressions.

Eddy diffusion values that were calculated with Yu's equation were plotted against a theoretical range of eddy diffusion values [Equation 4.2] (10). Fisher's equation gives a general estimate for eddy diffusion in a channel using the average tidal current speed and median depth across the study area [Equation 4.2]. The range in K_s values was calculated by changing the drag coefficient. Calculated K_s were found to be either within or below the theoretical bounds for all nine days [Figure 3.2].

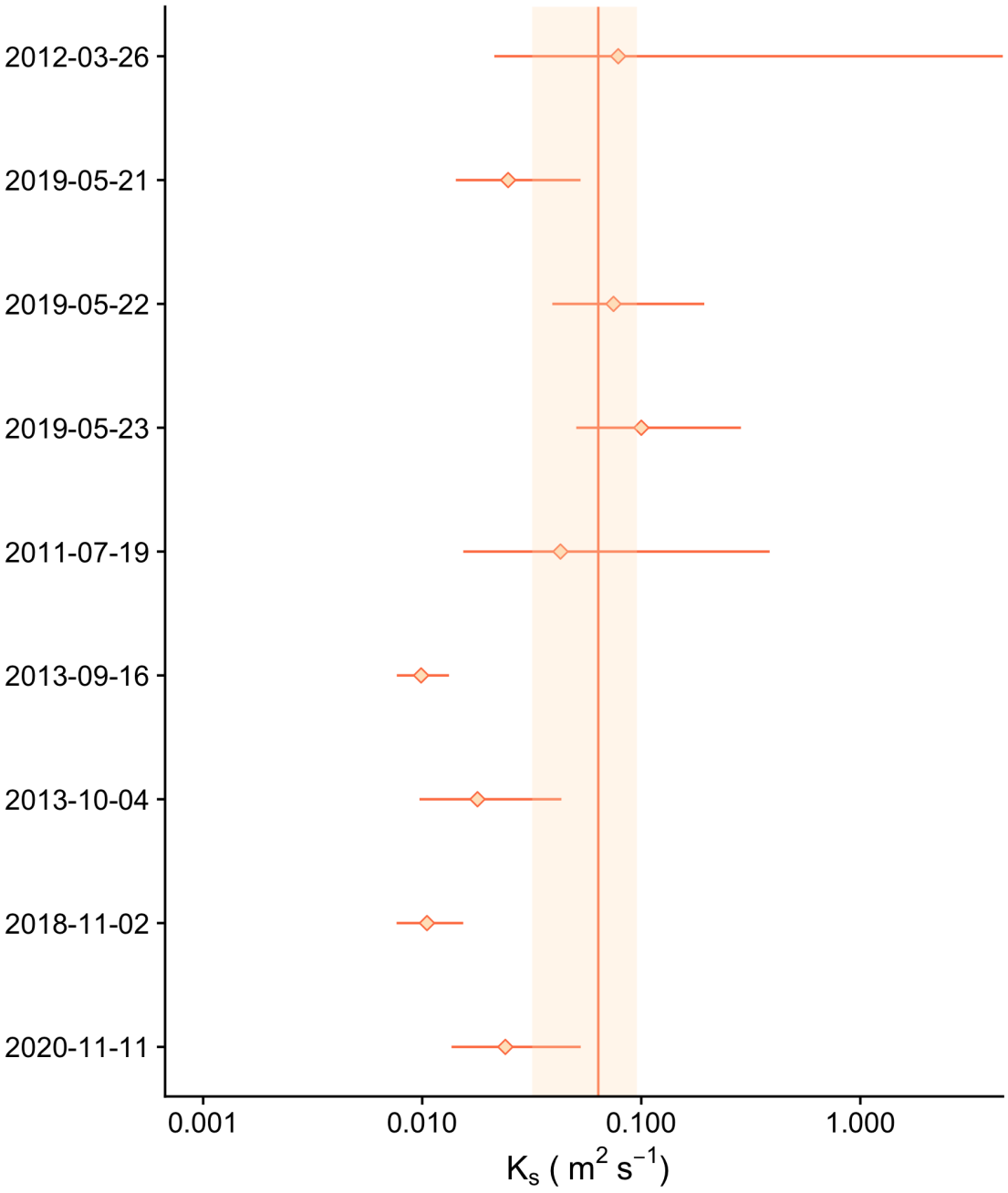

Figure 3.2: Estimated eddy diffusion coefficients for nine days based on the rate of change of phase lag with depth over the entire study box. The vertical line represents an average theoretical value for the eddy diffusion coefficient in an unstratified flow, using an average current speed of 0.75 m s^{-1}, the average regional depth of 19 m and a drag coefficient of 2.5×10^{-3} (31; 12). The edges of the box represent a range of the drag coefficient from 1-4 $\times 10^{-3}$. Dates organized by month to show seasonal trends.

Chapter 4

Discussion

On 9 of the 31 days identified as having 8 clear GOCI images, significant M4 variability in Rayleigh-corrected reflectance in the red band was observed in over 300 or more pixels. This result demonstrates both that reflectance in the region responds to tidally-induced resuspension and that GOCI is useful for characterizing tidal sediment dynamics (5; 23). Differences in fits among pixels were correlated with depth in a way consistent with a simplified numerical model of tidal resuspension (38). Intercepts, amplitudes and phases of the fits were inversely correlated with depth.

A larger intercept simply means that mean reflectance throughout the day was larger at that location. Intercepts were larger over ridges than channels. If the current speed and sediment size and supply are similar over channels and ridges, then the closer proximity of the sea surface to the seabed over ridges means that sediment concentration will be higher at the sea surface over ridges (38).

Amplitude represents how much surface reflectance changes throughout the day. Shallower regions reach larger sediment concentrations for the reasons stated above, but sediment sinking during slack water returns concentrations to background levels across the study area. Therefore variability is higher in shallower flows (38).

4.1 Phase Lag and Eddy Diffusion

For the 9 days with significant M4 variability, it is assumed that vertical eddy diffusion is responsible for bringing sediment that has been tidally resuspended to the water's surface. In a diffusive system the time required to cross a distance H is defined as (6)

$$\tau = \frac{H^2}{K_s} \tag{4.1}$$

In turbulent channel flow the vertical eddy diffusion coefficient scales as (10)

$$K_s \propto u_* * H, \tag{4.2}$$

where u_* is the shear velocity (m s^{-1}) and H is flow depth (m). The time required to diffuse from the seabed to the sea surface, therefore, scales as

$$\tau \propto \frac{H}{u_*} \tag{4.3}$$

Therefore, in turbulent channel flow the time required for resuspended sediment to reach the sea surface increases with increasing flow depth and decreases with increasing flow speed.

The observation that suspended sediment took longer to reach the surface over channels than ridges is consistent with the equation 4.1. Sediment takes longer to reach the surface in deeper flows. Equation 4.2 also demonstrates that if the flow is faster over ridges due to flow continuity, then diffusion time over ridges would be smaller (Equation 4.3).

The Yu et al. model is broadly consistent with the time and depth variation of reflectance in the image sets. Several significant simplifying assumptions, however, underlie this approach. Because K_s is calculated by taking the derivative of Yu's equation for phase as a function of depth , differences in K_s values were not calculated between a ridge and channel. Instead, the calculated value of eddy diffusion applies to the whole region using the median depth of 19 m. Current speed is assumed to be spatially uniform across the study area. In the Yu

model eddy diffusion is constant throughout the flow. Finally, sediment size, and therefore sediment settling velocity, were not accounted for in the equation relating phase to water depth (Equation 2.11). The equation's assumption is valid for regions with large current velocities and small settling velocities (38). The HMB has been characterized as a region with sediment sizes ranging between fine muds and fine sands, and experiences strong currents, meeting the requirements for this assumption (22; 21).

Eddy diffusion coefficients derived from application of Yu's model to the fitted values of phase as a function of depth were consistent with theoretical scaling from Fischer's equation 4.3. Despite the simplifications, the consistency of estimated and theoretical values of K_s is encouraging, and it suggests that remotely sensed observations of reflectance in tidal seas can be used constrain mixing dynamics.

The estimated values of K_s tended to be higher in the spring and summer, and lower in the fall. However, neither of the primary factors in Eq. 15 that affect eddy diffusion are likely to change seasonally. Water depth does not vary greatly throughout the year, and tidal currents likely do not depend on the season. If the two primary variables that determine eddy diffusion are consistent between days, then some other process must affect the rate of diffusion of sediment to the sea surface.

The factor that does change seasonally is the amount of available loose sediment over the HMB (22; 23). Two potential explanations for differences in seasonal behaviour due to the sediment budget change are seasonal increases of flocculation in the water column, and stratification of suspended sediment at depth.

Due to the increase in available sediment, flocculation at depth could be occurring in winter months. With higher SSC and flocculation occurring, sediment would settle faster out of the water column (20; 25). A higher settling velocity due to flocculation could increase upward phase lag (38). However, in a region as turbulent as the HMB, an increase in settling velocity is unlikely to produce an increase in phase lag because eddy diffusion is so large.

Waters over the HMB are well mixed, precluding stratification based temperature and

salinity (22; 21). Stratification can occur in high energy environments if there are very high concentrations of suspended sediment (7; 22). Sediment-induced stratification occurs when the vertical shear is insufficient to mix the density gradient produced by the higher concentration of suspended sediment near the seabed (33; 1). Because the vertical shears are large in the energetic tidal flow over the HMB, suspended sediment stratification requires dense concentrations of loose, fine-grained sediment. Sediment concentration in the summer may be inadequate to induce stratification, but significantly higher sediment concentrations in the winter may induce stratification and lead to the lower estimates for the eddy diffusion coefficient in fall and winter than in spring and summer.

A previous facies analysis has shown evidence of fluid muds, a byproduct of sediment-induced stratification, in cores of the HMB (4). Models have been created using a sedimentary bottom boundary layer in the water column around the HMB to predict tidal current patterns (1). Fieldwork conducted by Hill et al. in 2017 also found dense suspensions of sediment close to the seabed during peak tidal flow (13). These multiple lines of evidence suggest that seasonally-dependant sediment-induced density stratification occurs over the HMB.

4.2 Deviations from M4 Periodicity

Although 9 of the 32 days with 8 clear GOCI images showed significant M4 variability in reflectance, several did not. Lack of significant M4 variability arose either from alternate, non-tidal sediment resuspension processes, from non-particulate in-water constituents that affect Rayleigh-corrected reflectance but do not respond to tidal forcing, or from atmospheric variability over the course of a day that was not accounted for in the calculation of reflectance.

High winds and resulting strong wave action can suspend sediment independently from tidal currents. If winds and waves were high when an image was captured, GOCI would detect reflectance from sediment at the sea surface that was not introduced by tidal resuspension and mixing. This source of reflectance would degrade fits to an M4 periodic function.

Sufficiently high wind speeds and associated waves also can lower reflectance due to

sea foam forming on the water's surface (11). Sea foam is composed of both surficial and underwater bubbles, which scatter light in a similar manner to aerosols. Reflectance values affected by the bubbles cannot be corrected in the same way as changing atmospheric conditions, making surface reflectance at the time of image capture inaccurate, again degrading fits to an M4 periodic function (11).

Of the nine days with sufficient numbers of well fitted pixels, wind speeds were highest on March 26, 2012. Wind speeds that morning ranged between 6-8 m s^{-1} (19). The increased turbulence that morning compared to the other eight days selected could explain the wider range in derived K_s values (Fig. 3.2). Wind-derived turbulence may have brought high levels of sediment rather than high current speeds.

Finally, Rayleigh-corrected scattering accounts for only the molecular component of atmospheric scattering. Corrections for Rayleigh scattering do not account for diurnal changes in atmospheric scattering and absorption by aerosols across the study area. Aerosol optical depth and the concentration of aerosols smaller than 2.5 μm vary diurnally across the region (24). If aerosol levels changed during acquisition of an 8-image set, Rayleigh-corrected reflectance values through the day may have degraded correlation with the sediment concentration at the surface, leading to a poor pixel fit.

4.3 Future Work

This research supports the use of GOCI as a tool to investigate tidal sediment dynamics. More research, however, is required to examine the hypothesis that suspended sediment stratification increases the diffusion time required for resuspended sediment to reach the sea surface in fall and winter relative to spring and summer. Ideally, in situ profiles of suspended sediment and current velocity should be gathered over the HMB on a clear day in order to compare in situ measurements with GOCI imagery. Measurements should be taken over both a ridge and channel, to help understand how suspended sediment behaves in response to tidal currents and at different depths. Ideally, two excursions, one in the summer and another in the winter

should be conducted. These data would help to test the hypothesis that suspended sediment stratification occurs seasonally.

Analysis of other sites that have similar banded reflectance that corresponds with bathymetry would be valuable in developing greater understanding of this phenomenon [Figures 1.1 - 1.3]. As GOCI has historically been the only geostationary ocean colour satellite with such a high temporal and spatial resolution, the obvious next site to study would be Gyeonggi Bay, located approximately 300 km up the South Korean coast from the HMB [Figure 1.3]. This site falls within GOCI's image capture range, and so could be studied with similar methodology to that used in this research. In future analyses, imagery after the end of GOCI's life cycle can be obtained by GOCI II, which was launched onboard the GEO-KOMPSAT-2B satellite in 2020 and will be in operation until 2031 (35). GOCI II will have the same image frequency, with an increased spatial resolution, image area, and number of bands (35).

Other satellite platforms may be able to extend the geographic range of the type of temporal analysis of tidal resuspension used here. Weather satellites may be useful as a source of high-frequency imagery when expanding beyond GOCI's field of view. While most weather satellites have a coarser spatial resolution than GOCI, they also take multiple images per day over the same region, perhaps allowing for a similar analysis of surficial patterns throughout a tidal cycle. Researchers have been able to track and model surface ocean currents using high frequency weather satellite data around both North America and the West Sea (36). Weather satellites have also estimated ocean colour, allowing for analysis of the evolution large-scale patterns of ocean chromaticity at temporal resolutions under an hour (15). These strategies show promise in the ability to extend the methodology used in this paper to other macrotidal regions to compare surficial reflectance and tidal cycles.

Chapter 5

Conclusion

GOCI can track regional dynamic patterns in SSC within a semidiurnal tidal cycle, and observed patterns of reflectance correlate with bathymetry. Shallow waters over the HMB have higher surficial concentrations of suspended sediment throughout a tidal cycle. Deep waters have lower surficial SSC, and channels often have a significant delay in peak reflectance compared to ridges (Figures 3.1, 2.3).

Based on reflectance data from nine clear days with significant M4 tidal variability, a relationship between derived K_s values and time of year may exist. Estimated eddy diffusion coefficients trend lower during the winter, when increased turbulence and wind speeds bring more suspended sediment to the region. The lower estimated K_s during periods of high SSC may be linked to sediment-induced density stratification during fall and winter, when suspended sediment concentrations in the region are higher due to the effects of the monsoonal climate. These results suggest that GOCI may be able to infer subsurface tidal dynamics based on surface reflectance patterns.

More data is needed in order to examine the seasonal variability in eddy diffusion coefficients proposed in this thesis. Fieldwork is needed, ideally on days with low wind speed during both the summer and winter over a tidal ridge and channel of the HMB. In situ observation would help in testing the hypothesis that seasonal differences in sediment concentration alter flow

dynamics in tidal channels by suppressing upward mixing of dense suspensions in fall and winter.

Bibliography

[1] BYUN, D., AND WANG, X. H. The effect of sediment stratification on tidal dynamics and sediment transport patterns. *Journal of Geophysical Research 110* (2005).

[2] CARBAJAL, N., MONTAÑO-LEY, Y., SOTO-JIMÉNEZ, M., PÁEZ-OSUNA, F., AND TUXPAN, J. Finger-like plumes of suspended sediment in the colorado river delta, gulf of california. *Estuarine, Coastal and Shelf Science 245* (2020).

[3] CENTER, N. G. S. F. Ocean ecology laboratory, ocean biology processing group. portable remote imaging spectrometer (prism) ocean color data.

[4] CHANG, T. S., HA, H. J., AND CHUN, S. S. Factors controlling mud accumulation in the heuksan mud belt off southwestern korea. *Geo-Marine Letters 35* (2015).

[5] CHOI, J.-K., PARK, Y. J., AHN, J. A., LIM, H.-S., EOM, J., AND RYU, J.-H. Goci, the world's first geostationary ocean color observation satellite, for the monitoring of temporal variability in coastal water turbidity. *Journal of Geophysical Research 117* (2012).

[6] COSTIGLIOLA, L., HEYES, D. M., SCHRØDER, T. B., AND DYRE, J. C. Revisiting the stokes-einstein relation without a hydrodynamic diameter. *The Journal of Chemical Physics 150 (2)* (2019).

[7] EGAN, G., M. A. J. C.-G. F. O. . M. S. Sediment-induced stratification in an estuarine bottom boundary layer. *Journal of Geophysical Research: Oceans 125* (2020).

[8] EGBERT, G. D., AND EROFEEVA, S. V. Efficient inverse modeling of barotropic ocean tides. *Journal of Atmospheric and Oceanic Technology 19.2* (2002), 183–204.

[9] EVANS, C. Determining subsurface suspended sediment mechanisms through surficial remote sensing techniques, south korea, 2019.

[10] FISCHER, H., LIST, E., KOH, R., IMBERGER, J., AND BROOKS, N. *Mixing in Inland and Coastal Waters*. Academic Press, Inc., 1979.

[11] FROUIN, R., SCHWINDLING, M., AND DESCHAMPS, P.-Y. Spectral reflectance of sea foam in the visible and near-infrared: In situ measurements and remote sensing implications. *Journal of Geophysical Research 101* (1996), 14361–14371.

[12] GEBCO COMPILATION GROUP. Gebco gridded bathymetry data. https://www.gebco.net/data$_a nd_p roducts/gridded_b athymetry_d ata/$, 2020.

[13] HILL, P. S. Personal communications, 2017.

[14] HWANG, S., AND JO, C. H. Tidal current energy resource distribution in korea. *Energies 12* (2019).

[15] JOLLIFF, K., LEWIS, D., LADNER, S., AND CROUT, L. Observing the ocean submesoscale with enhanced-color goes-abi visible band data. *Sensors 19* (2019).

[16] KANG, J. W., MOON, S.-R., PARK, S.-J., AND LEE, K.-J. Analyzing sea level rise and tide characteristics change driven by coastal construction at mokpo coastal zone in korea. *Ocean Engineering 36* (2009), 415–425.

[17] KIM, B.-J., KRIPALANI, R. H., AND OH, J.-H. AMD MOON, S.-E. Summer monsoon rainfall patterns over south korea and associated circulation features. *Theoretical and Applied Climatology 72* (2002), 65–72.

[18] KOENKER, R. *Quantile Regression*. Econometric Society Monographs. Cambridge University Press, 2005.

[19] KOREAN METEOROLOGICAL ADMINISTRATION. Ndbc - station 22102 recent data.

[20] LAW, B., MILLIGAN, T., HILL, P., AND BUGDEN, G. The effect of concentration on particle settling in the minas basin, nova scotia. *Continental Shelf Research 223* (05 2021), 104448.

[21] LEE, H. J. A review on the holocene evolution of an inner-shelf mud deposit in the southeastern yellow sea: the huksan mud belt. *Ocean Science Journal 50*, 4 (2015), 615–621.

[22] LEE, H. J., AND CHU, Y. S. Origin of inner-shelf mud deposit in the southeastern yellow sea: Huksan mud belt. *Journal of Sedimentary Research 71* (2001), 144–154.

[23] LEE, Y.-K., CHOI, J.-K., AND LEE, H. J. A study on seasonal dynamics of suspended particulate matter in korean coastal waters using goci. *Journal of Coastal Research* (2020), 232–245.

[24] LENNARTSON, E. M., WANG, J., GU, J., CASTRO GARCIA, L., GE, C., GAO, M., CHOI, M., SAIDE, P. E., CARMICHAEL, G. R., KIM, J., AND JANZ, S. J. Diurnal variation of aerosol optical depth and $pm_{2.5}$ in south korea: a synthesis from aeronet, satellite (goci), korus-aq observation, and the wrf-chem model. *Atmospheric Chemistry and Physics 18*, 20 (2018), 15125–15144.

[25] MILLIGAN, T., HILL, P., AND LAW, B. Flocculation and the loss of sediment from the po river plume. *Continental Shelf Research 27* (02 2007), 309–321.

[26] PADMAN, L., AND EROFEEVA, S. *Tidal Model Driver (TMD) Manial*, 2005. Version 1.2.

[27] QIU, Z., ZHENG, L., ZHOU, Y., SUN, D., WANG, S., AND WU, W. Innovative goci algorithm to derive turbidity in highly turbid waters: A case study in the zhejiang coastal area. *Optics Express 23*, 19 (2015), A1179–A1193.

[28] ROOS, P. C., WEMMENHOVE, R. AMD HULSCHER, S. M. H., HOEIJMAKERS, W. M., AND KRUYT, N. Modeling the effect of nonuniform sediment on the dynamics of offshore tidal sandbanks. *Journal of Geophysical Research 112*, FO2011 (2007).

[29] RUDDICK, K., VANHELLEMONT, Q., YAN, J., NEUKERMANS, G., WEI, G., AND SHANG, S. Variability of suspended particulate matter in the bohai sea from the geostationary ocean color imager (goci). *Ocean Science Journal 47* (2012), 331–345.

[30] RYU, J.-H., HAN, H.-J., CHO, S., PARK, Y.-J., AND AHN, Y.-H. Overview of geostationary ocean color imager (goci) and goci data processing system (gdps). *Ocean Science Journal 47*, 3 (2012), 223–233.

[31] SOULSBY, R. Chapter 5 the bottom boundary layer of shelf seas. In *Physical Oceanography of Coastal and Shelf Seas*, B. Johns, Ed., vol. 35 of *Elsevier Oceanography Series*. Elsevier, 1983, pp. 189–266.

[32] THUILLIER, G., HERSÉ, M., SIMON, P. C., LABS, D., MANDEL, H., GILLOTAY, D., AND FOUJOLS, T. The visible solar spectral irradiance from 350 to 850 nm as measured by the solspec spectrometer during the atlas i mission. *Solar Physics 177*, 1 (1998), 41–61.

[33] TROWBRIDGE, J. H., AND KINEKE, G. C. Structure and dynamics of fluid muds on the amazon continental shelf. *Journal of Geophysical Research 99* (1994), 865–874.

[34] VANHELLEMONT, Q., AND RUDDICK, K. Turbid wakes associated with offshore wind turbines observed with landsat 8. *Remote Sensing of Environment 145* (2014), 105–115.

[35] WORLD METEOROLOGICAL ASSOCIATION. Details for instrument goci-ii. https://space.oscar.wmo.int/instruments/view/goci$_i i$, 2021. $Accessed : 2022 - 10 - 03$.

[36] YANG, H., ARNONE, R., AND JOLLIFF, J. Estimating advective near-surface currents from ocean colour satellite images. *Remote Sensing of Environment 158* (2015), 1–14.

[37] YI, S. Holocene vegetation responses to east asian monsoonal changes in south korea. *Climate Change - Geophysical Foundations and Ecological Effects* (09 2011).

[38] YU, Q., FLEMMING, B., AND GAO, S. Tide-induced vertical suspended sediment concentration profiles: Phase lag and amplitude attenuation. *Ocean Dynamics 61* (04 2011), 403–410.